PAPER

CrossMark
click for updates

Preparation of network-like ZnO–FeWO$_4$ mesoporous heterojunctions with tunable band gaps and their enhanced visible light photocatalytic performance†

Yongchao Ma, Yunhua Guo, Haiyan Jiang, Dan Qu, Jing Liu, Wukui Kang, Ying Yi, Wei Zhang, Jinsheng Shi and Zhongzhi Han*

Novel mesoporous ZnO–FeWO$_4$ (Zn–FeWO$_4$) heterojunctions with network-like structure were synthesized with a combination of thermal decomposition and hydrothermal methods. The samples were characterized by X-ray diffraction (XRD), scanning electron microscopy (SEM), transmission electron microscopy (TEM), X-ray photoelectron spectroscopy (XPS), N$_2$ sorption and Brunauer–Emmett–Teller (BET) surface area analysis, diffuse reflection spectroscopy (DRS) and photoluminescence spectroscopy (PL). The results showed that the size of FeWO$_4$ was reduced by the modification of ZnO. With the increasing molar ratio of ZnO to FeWO$_4$, the quantum size of FeWO$_4$ decreased from 11 nm to 4 nm, as is followed by a surprisingly band gap broadening. Photocatalytic activity toward the degradation of RhB under visible light irradiation was investigated. The optimum decomposition rate of RhB using the prepared 1.5Zn–FeWO$_4$ heterojunction was almost 39 and 9.7 times that of pristine ZnO and FeWO$_4$, respectively. The active species trapping experiments showed that the holes exhibited an obvious influence on the photocatalytic degradation process. The study on the mechanism showed that the enhanced photocatalytic activity was mainly ascribed to heterojunction construction and band gap broadening, which enhance the efficient transfer and the oxidation potential of holes. This heterojunction shows a potential industrial application to remove undesirable organics from the environment.

1. Introduction

In recent years, semiconductor photocatalysis has attracted considerable interest because it provides a promising pathway for solving environmental pollution and energy shortage.[1–4] Metal tungstates belong to an important family of semiconductors with potential application in various fields, such as in catalysis,[5] photoluminescence,[6] microwave application[7] and humidity sensors.[8] Among various metal tungstates, monoclinic ferrous tungstate (FeWO$_4$) is an indirect band gap semiconductor with a narrow band gap of 1.8–3.0 eV,[9,10] which matches the solar visible spectrum well. Recently, Yu *et al.* firstly reported the photocatalytic degradation activity of FeWO$_4$ under modeling sunlight in 2009.[11] Kuang *et al.* reported the photocatalytic decomposition activity of spindle-like FeWO$_4$ nanoparticles under UV irradiation.[12] However, the visible light photocatalytic

efficiency of FeWO$_4$ is not ideal because of the poor quantum yield caused by the rapid recombination of photogenerated electrons and holes. Thus, it is of considerable significance to develop an efficient strategy to promote the separation efficiency of internal charge carriers of FeWO$_4$ photocatalysts.

As a result, many attempts have been made to overcome these disadvantages, including controlling the morphology,[10,11] and forming composite structures or heterojunctions.[13,14] Construction of a heterostructure photocatalyst might be an effective way to enhance the visible light photocatalytic activity of FeWO$_4$, such as FeWO$_4$–TiO$_2$[13] and FeWO$_4$–Fe$_3$O$_4$.[14] The enhanced photocatalytic activity of the composites was ascribed to the improvement of charge separation and the interfacial charge transfer efficiency.[15,16] It is well known that ZnO has been recognized as an excellent material for the photocatalytic process because of its high photosensitivity, low cost and nontoxic nature.[17,18] To date, some novel photocatalysts have been developed by coupling ZnO with other semiconductors, such as g-C$_3$N$_4$–ZnO,[19] CdS–ZnO heteroarchitecture,[20] Cu$_2$O–ZnO,[21] SnO$_2$–ZnO heterojunction,[22] ZnO–BiOI,[23] and BiVO$_4$–ZnO.[24] The ZnO-based heterojunction exhibited enhanced photocatalytic activity originating from the efficient separation

*Qingdao Agricultural University, Qingdao 266109, People's Republic of China.
E-mail: hanzhongzhiqn@aliyun.com; Fax: +86-532-86080213;
Tel: +86-532-88030161*

† Electronic supplementary information (ESI) available. See DOI: 10.1039/c5nj00900f

and transfer of charge carriers. Motivated by these efforts, we intend to design a ZnO–FeWO$_4$ heterojunction to enhance the visible light photocatalytic activity of FeWO$_4$. By calculating the energy band positions of ZnO and FeWO$_4$, it was found that the energy levels of FeWO$_4$ and ZnO are well-matched, suiting to construct a heterojunction with efficient electron–hole separation ability. However, to the best of our knowledge, there is no report on the fabrication of ZnO–FeWO$_4$ heterostructures with efficient photocatalytic activity under visible light irradiation.

Herein, ZnO–FeWO$_4$ mesoporous heterojunctions with network-like structure were, for the first time, prepared by a simple thermal decomposition followed by a hydrothermal process. The modification of ZnO reduced the size of FeWO$_4$, which can significantly tune the band gaps of ZnO–FeWO$_4$ composites. The excellent photocatalytic activity of ZnO–FeWO$_4$ heterojunctions was evaluated by degrading RhB under visible light irradiation. The active species trapping experiments showed that the holes played an important role in the photocatalytic degradation process. In addition, the ZnO–FeWO$_4$ heterojunction also exhibited high stability and durability after four successive cycles. Finally, the possible photocatalytic mechanism of this heterojunction was proposed based on the investigation of reactive species and the band structure of FeWO$_4$ and ZnO.

2. Experimental

2.1. Material synthesis

All the reagents were purchased from Sinopharm Chemical Reagent Co., Ltd and used directly for experiments without any further purification. Deionized water was used throughout this study. The ZnO sample was synthesized by a facile thermal treatment.[11] Briefly, an appropriate amount of $(ZnCO_3)_2 \cdot [Zn(OH)_2]_3$ was calcinated at 280 $^{\circ}$C in a muffle furnace for 3 h with a heat rate of 10 $^{\circ}$C min^{-1}. After being cooled to room temperature, the obtained white products were washed by absolute ethanol and distilled water three times and then dried at 60 $^{\circ}$C overnight.

ZnO–FeWO$_4$ composites were synthesized through a modified solvothermal method.[11] Briefly, an appropriate amount of ZnO was dispersed in a mixed solution with 3.5 mL of distilled water and 63 mL of ethylene glycol with ultrasonication for 30 min. Then, 5 mmol of FeCl$_3 \cdot$6H$_2$O was added to the ZnO suspension and stirred magnetically for 30 min. Subsequently, 5 mmol of Na$_2$WO$_4 \cdot$2H$_2$O dissolved in 3.5 mL of distilled water was dropwise added to the above mixture. 10 mmol of sodium acetate was then added to the above mixture with continuous stirring. After 30 min stirring, the above suspension was transferred into a stainless steel autoclave (100 mL) with a Teflon liner and heated at 200 $^{\circ}$C for 12 h. After being cooled to room temperature naturally, the obtained products were separated and washed with absolute ethanol and distilled water and then dried at 60 $^{\circ}$C for 6 h. The molar ratio of ZnO to FeWO$_4$ in the as-prepared composites was 0.5, 1, 1.5, and 2. And the corresponding samples were denoted 0.5Zn–FeWO$_4$, 1Zn–FeWO$_4$, 1.5Zn–FeWO$_4$ and 2Zn–FeWO$_4$, respectively.

For comparison, the pure FeWO$_4$ sample was prepared in the absence of ZnO under the same conditions. To evaluate the effect of the heterojunction on the photocatalytic activity of Zn–FeWO$_4$ heterostructures, a mechanically mixed FeWO$_4$ and ZnO sample (M-1.5Zn–FeWO$_4$) was prepared.

2.2. Material characterization

The crystalline phases of Zn–FeWO$_4$ composites were recorded by X-ray diffraction (XRD) using a Bruker D8 diffractometer (Cu Kα radiation, λ = 0.15406 nm). The morphology and structure of the as-prepared samples was examined using a scanning electron microscope (SEM, S-4800, Hitachi) and a transmission electron microscope (TEM, JOEL JEM 2001). X-ray photoelectron spectra (XPS) of the catalysts were recorded on an ESCA-3 Mark II spectrometer (VG Scientific Ltd, England) using Al Kα (1486.6 eV) radiation. Ultraviolet visible (UV-vis) diffuse reflection spectra were measured by means of a UV-vis spectrophotometer (TU-1901, China), which involves an integrating sphere attachment in the range of 200 to 800 nm. BaSO$_4$ was used as the reflectance standard material. The photoluminescence (PL) spectra of the samples were recorded on a Hitachi F-4600 fluorescence spectrophotometer to observe the recombination rate of electron–hole pairs. All of the measurements were performed at room temperature.

2.3. Photocatalytic test

The photocatalytic activities of the as-prepared products were evaluated by the degradation of RhB dye under visible light irradiation. The photocatalytic reactor (PLS-SXE 300, Beijing Perfect light Co., Ltd) consists of a quartz glass with a circulating water jack and a 300 W Xe lamp with a 420 nm cutoff filter. Typically, an aqueous solution of RhB (100 mL, 10^{-5} M) was placed in a glass, and 30 mg photocatalyst was added. Prior to irradiation, the suspensions were magnetically stirred in the dark for about 60 min to obtain a good adsorption–desorption equilibrium. At 30 min intervals, 5 mL of the solution was taken out and centrifuged to remove the photocatalyst. Then, the filtrates were analyzed by recording variations of the absorption band maximum (553 nm) in the UV-vis spectra of RhB using a TU-1901 spectrophotometer.

2.4. Active species trapping and radical quantification experiments

To detect the active species generated in the photocatalytic process, various scavengers including isopropyl alcohol (IPA, 10 mmol L^{-1}), p-benzoquinone (p-BQ, 1 mmol L^{-1}), and triethanolamine (TEOA, 10 mmol L^{-1}) were introduced into the solution of RhB.[25] The other photocatalytic process was the same as the former photocatalytic activity test (Section 2.3).

2.5. Photoelectrochemical measurements

The photoelectrochemical characteristics were measured in a CHI660D electrochemical working station using a standard three-compartment cell under Xe arc lamp irradiation with 300 W. In a typical procedure, a commercial ITO glass (1.0 × 1.0 cm^2) was ultrasonicated in an ethanol and distilled water

bath prior to use. The clean ITO glass substrate was then immersed in the slurry of the as-prepared photocatalyst (3 mg) and ethanol (3 mL) mixtures. The substrate was then vacuum-dried at 80 °C to eliminate ethanol and subsequently maintained at 100 °C overnight. An ITO glass coated with the as-prepared samples, a piece of Pt sheet, a saturated calomel electrode (SCE) and 0.01 M Na_2SO_4 were used as the working electrode, the counter electrode, the reference electrode and the electrolyte, respectively.

3. Results and discussion

The network-like ZnO–$FeWO_4$ mesoporous heterojunction photo-catalysts with tunable band gaps have been synthesized *via* a two-step route. ZnO nanoparticles were first obtained by calcination of the corresponding precursors. After that Zn–$FeWO_4$ hetero-junctions were prepared with a solvothermal treatment.

3.1. Characterization of samples

Fig. 1 presents the XRD patterns of the as-prepared $FeWO_4$, ZnO, and ZnO modified $FeWO_4$ samples. As shown in Fig. 1a and f, all the diffraction peaks can be well indexed to mono-clinic $FeWO_4$ (JCPDS card no. 46-1446) and hexagonal ZnO (JCPDS card no. 36-1451), respectively. Besides, no traces of other phases are discovered, indicating the high purity of the samples. For the modified products, the XRD peaks of mono-clinic $FeWO_4$ and hexagonal ZnO were observed, confirming the coexistence of ZnO and $FeWO_4$. After modification with ZnO, all the diffraction peaks become broader and weaker, confirming the formation of the nanostructure material.[26] Moreover, the decreased peak intensity of the ZnO modified $FeWO_4$ products indicates the crystal growth inhibition effect between ZnO and $FeWO_4$.[27]

In order to obtain detailed information about the morpho-logy and the nanostructure of the ZnO modified $FeWO_4$ sample, SEM and TEM observations were carried out, and the results are shown in Fig. 2. A typical SEM image (Fig. 2a) shows that the
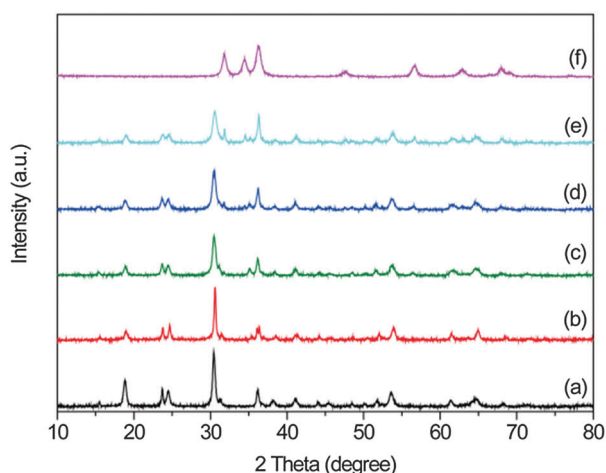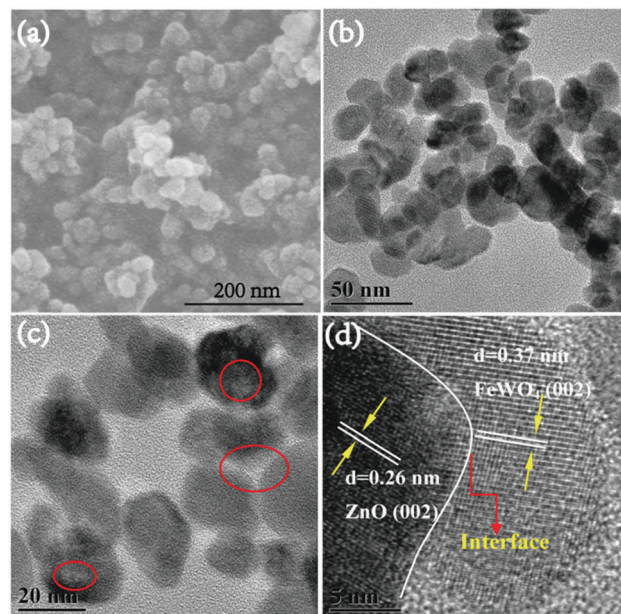

Fig. 2 (a) SEM image, (b) TEM image and (c, d) HRTEM images of the as-synthesized 1.5Zn–$FeWO_4$ heterojunction.

$1.5Zn$–$FeWO_4$ composite is composed of numerous nano-particles with a diameter size in the range of about 10–40 nm. The morphologies of the obtained ZnO, $FeWO_4$, 0.5Zn–$FeWO_4$, 1Zn–$FeWO_4$ and 2Zn–$FeWO_4$ samples are shown in Fig. S1 (ESI†). Interestingly, compared to the nanoplates of $FeWO_4$, the shapes of Zn–$FeWO_4$ composites are much tiny nanospheres. A low-magnified TEM image of the 1.5Zn–$FeWO_4$ composite shows that the sample has nanosphere morphology with a network structure, as presented in Fig. 2b. Furthermore, in order to confirm the relative location of ZnO and $FeWO_4$ nanoparticles, we made the cross-sectional compositional line profiles of the 1.5Zn–$FeWO_4$ heterojunction (Fig. S2, ESI†). Fig. S2c (ESI†) shows the EDS analysis results on the place defined by the small yellow square in Fig. S2a (ESI†), confirming the existence of Fe, W, Zn and O in this area. Besides, the line profiles of the corresponding composi-tions (Fig. S2e and f, ESI†) on the small yellow square reveal the distribution of Zn in the left location and an increase of Fe in the right location. It is worth noting that each nanoparticle attaches to several other nanoparticles and no self-nucleated and isolated $FeWO_4$ is observed, indicating the formation of Zn–$FeWO_4$ hetero-junctions. A typical high-resolution TEM image of Zn–$FeWO_4$ heterojunctions is shown in Fig. 2c and d. It can be clearly observed that holes with a size of about 3 nm on the surface of ZnO nanocrystals and some same pores between nanoparticles (highlighted by circles) indicate the mesoporous nature of Zn–$FeWO_4$ heterojunctions. An interface region was observed in the heterostructures, indicating an intimate contact between the ZnO and $FeWO_4$ nanoparticles (Fig. 2d). The adjacent lattice spacings of the planes are *ca.* 0.26 and 0.37 nm, corresponding to the (002) planes of hexagonal wurtzite ZnO and (002) planes of monoclinic $FeWO_4$, respectively. There are some nano-particles on the surface of the ZnO nanocrystals, and the exposed surface of ZnO is easily observed in Fig. 2d.

Fig. 1 XRD patterns of the as-prepared samples: (a) $FeWO_4$, (b) 0.5Zn–$FeWO_4$, (c) 1Zn–$FeWO_4$, (d) 1.5Zn–$FeWO_4$, (e) 2Zn–$FeWO_4$, and (f) ZnO.

Compared to the FeWO$_4$ nanoplate, FeWO$_4$ in the Zn–FeWO$_4$ composites exhibits a smaller particle size (shown in Fig. S1, ESI†), which is attributed to the following reasons: (1) in the nucleation process, due to the existence of ZnO, which is employed as a high surface template, the reactants disperse uniformly on its surface. Instead of homogeneous nucleation, the heterogeneous nucleation occurs, which can inhibit the crystal growth. (2) In the process of hydrothermal reaction, the primarily formed crystalline grains distribute uniformly on the surface of ZnO, which can inhibit the further growth of the crystals.[28]

The chemical composition and surface chemical states of the as-obtained 1.5Zn–FeWO$_4$ was investigated by XPS, and the corresponding results are shown in Fig. 3. Fig. 3a shows the full spectrum of XPS of the prepared 1.5Zn–FeWO$_4$. The main peaks at 710.9, 35.5, 283.6, 1021.7 and 530.7 eV can be attributed to the binding energies of Fe 2p, W 4f, C 1s, Zn 2p and O 1s, respectively. The presence of carbon is mainly from pump oil due to vacuum treatment before the XPS test. In Fig. 3b, the peak values at 710.4 and 723.9 eV are assigned to the binding energies of Fe 2p$_{3/2}$ and Fe 2p$_{1/2}$, respectively. In Fig. 3c, two peaks located at 35.5 and 37.8 eV are assigned to W 4f with binding energies corresponding to those of tungsten in the formal valence of +6. From Fig. 3d, it can be observed that the XPS spectrum of Zn 2p shows two individual peaks positioned at 1021.7 and 1044.8 eV, which are assigned to Zn 2p$_{3/2}$ and Zn 2p$_{1/2}$, respectively.[24]

The N$_2$ adsorption and desorption measurement was used to study the Brunauer–Emmett–Teller (BET) surface areas and porosity of the as-prepared samples. Fig. 4 displays the typical N$_2$ adsorption–desorption isotherm of FeWO$_4$ and 1.5Zn–FeWO$_4$. As shown in Fig. 4, the N$_2$ sorption isotherm of FeWO$_4$ and 1.5Zn–FeWO$_4$ is characteristic of type IV with a clear hysteresis loop, suggesting their mesoporous properties.[29] In addition, the insets in Fig. 4 show the pore size distribution of FeWO$_4$ and 1.5Zn–FeWO$_4$. It can be seen that the pore was mainly distributed in the range of 8–40 nm, in agreement with the mesoporous structure. The N$_2$ adsorption–desorption

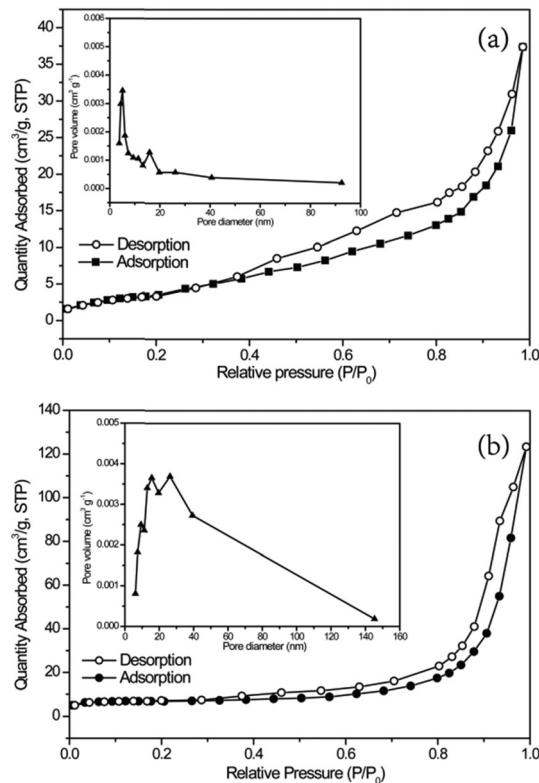Fig. 4 N$_2$ adsorption–desorption isotherms of (a) FeWO$_4$ sample and (b) 1.5Zn–FeWO$_4$ heterojunction. Inset: pore size distributions of the prepared samples.

isotherm of other Zn–FeWO$_4$ composites are shown in Fig. S3 (ESI†). BET surface area (S_{BET}) and the corresponding average pore diameter of the FeWO$_4$ and Zn–FeWO$_4$ products are listed in Table S1 (ESI†). The mesoporous structure is beneficial to the adsorption and transition of RhB or its intermediates during the photocatalytic process.

The optical properties of ZnO, FeWO$_4$, and Zn–FeWO$_4$ heterojunctions were investigated by UV-vis diffuse reflectance spectra, as shown in Fig. 5. The strong absorbance of the white ZnO nanoparticles began at around 400 nm, while the brown FeWO$_4$ sample exhibited profound adsorption over the entire visible light region. The fitting directed band gap of ZnO was determined to be 3.2 eV (Fig. S4, ESI†). It is noted that the Zn–FeWO$_4$ composites showed a broad and strong absorbance from 800 nm to the UV region, indicating the effective photo-absorption of this special structure composition. The indirect band gaps of the FeWO$_4$ and ZnO modified FeWO$_4$ are shown in Fig. 5b. With the increasing molar ratio of ZnO, the band gaps of Zn–FeWO$_4$ heterostructures show blue shift (Table S2, ESI†), which are attributed to the quantum confinement of FeWO$_4$ nanoparticles. On the basis of the effective mass approximation model, blue shift of FeWO$_4$ nanoparticles relative to the bulk is dominated by confinement of electrons and holes, as described by the following equation:[30]
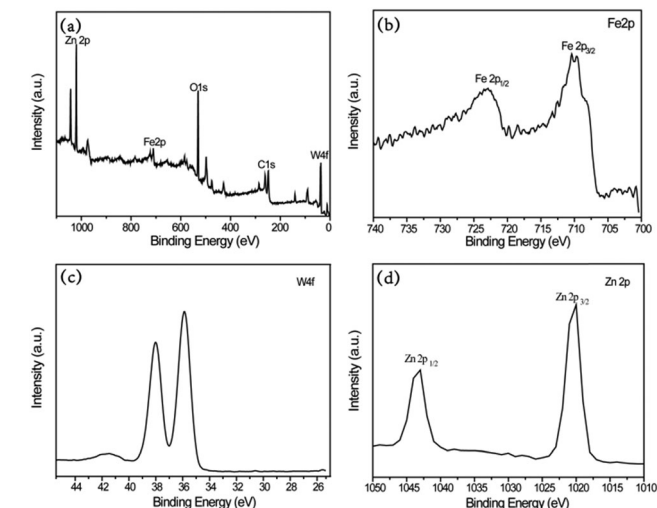

Fig. 3 XPS spectra of the as-obtained 1.5Zn–FeWO$_4$ products: (a) XPS full spectrum, (b) Fe 2p, (c) W 4f, and (d) Zn 2p.

$$\Delta E_g(R) = \frac{h^2}{8m_0 R^0}\left(\frac{1}{m_e^*} + \frac{1}{m_h^*}\right) \quad (1)$$

Fig. 6 Photoluminescence (PL) spectra measured at room temperature for FeWO₄ and ZnO modified FeWO₄ composite photocatalysts. The excitation wavelength was 210 nm.
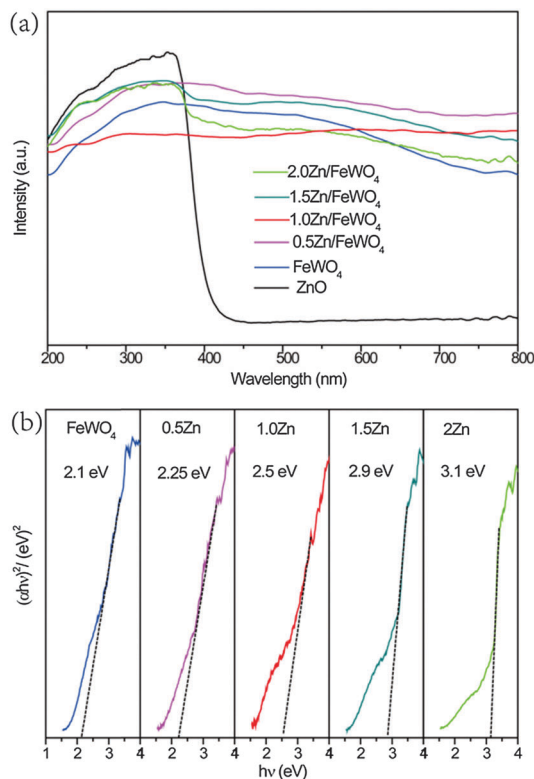
Fig. 5 (a) UV-vis diffuse reflectance spectra of the as-obtained samples. (b) Kubelka–Munk (KM) plot of FeWO₄ and FeWO₄–ZnO hybrid materials.

Fig. 7 Photocurrents of the as-prepared samples (a) FeWO₄, (b) ZnO, and (c) 1.5Zn–FeWO₄ with UV-vis light on–off cycles.

where $\Delta E_g(R)$ is the band gap shift for the crystal radius R, h the Planck's constant, m_0 the electron mass, while m_e^* and m_h^* are the effective mass of the electrons and holes, respectively. According to the above equation, the calculated sizes of FeWO₄ in the Zn–FeWO₄ composites range from 11 to 4 nm (Fig. S5, ESI†).

The immigration, transfer, and recombination of photo-generated electrons and holes in the Zn–FeWO₄ heterostructures were confirmed by PL emission spectra at room temperature, as shown in Fig. 6. All the samples displayed a broad emission band in both the UV and visible region ranging from 330 nm to 600 nm. After ZnO was introduced, the PL emission intensity of FeWO₄ decreased. This may be ascribed to the increase in trap states on the surface defect of Zn–FeWO₄ heterostructures.[31] Besides, the visible emission at about 480 nm is the characteristic near-band-edge emission due to the recombination of the free photo-generated electrons and holes.[32] Furthermore, 1.5Zn–FeWO₄ and 2Zn–FeWO₄ were found to show higher UV emission (indicated by a steep increase in the UV region) than 0.5Zn–FeWO₄ and 1Zn–FeWO₄. This result indicates the improved crystallinity of ZnO in 1.5Zn–FeWO₄ and 2Zn–FeWO₄ composites, which is consistent with XRD results.[33] The PL results confirm the importance of the heterojunctions in efficient charge separation.

The effective separation of electron–hole pairs in 1.5Zn–FeWO₄ was also confirmed by the photocurrent measurement of photocatalyst electrodes (Fig. 7). It can be clearly seen that rapid and consistent photocurrent responses are observed during on and off cycles of irradiation. It is worth noting that
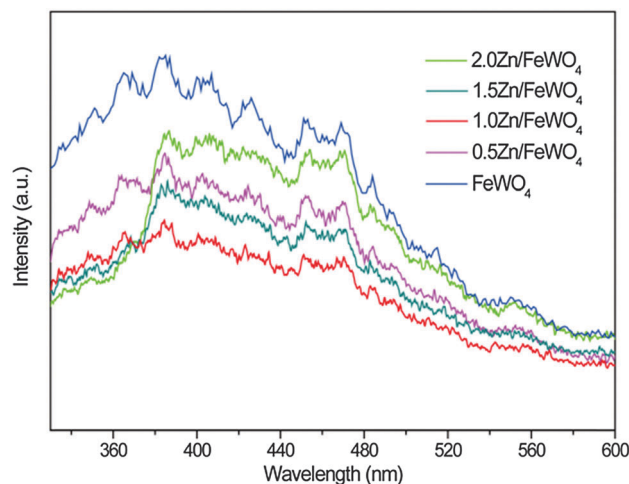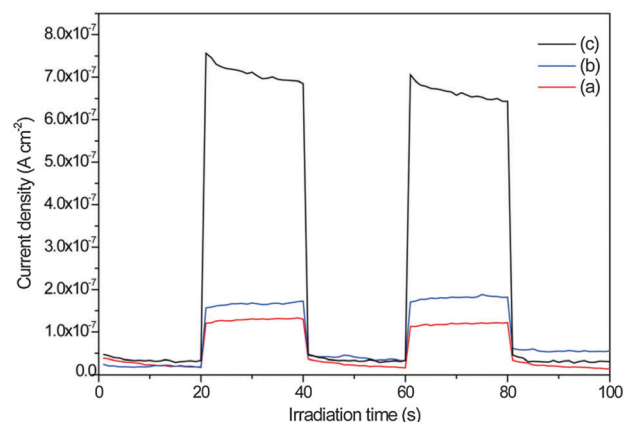
the photocurrent density of the 1.5Zn–FeWO₄ heterostructure electrode is higher than that of the pure ZnO and FeWO₄ electrode, respectively. The enhanced photocurrent response of the as-prepared mesoporous 1.5Zn–FeWO₄ heterostructure indicates higher separation efficiency of the photoinduced electron–hole pairs and a lower recombination rate in such hybrid structures under light illumination. This can be explained by close interfacial connections and the synergetic effect existing in the 1.5Zn–FeWO₄ interface.

3.2. Photocatalytic performance

The photocatalytic activities of ZnO, FeWO₄ and Zn–FeWO₄ heterojunctions were tested by the degradation of RhB solution under visible light irradiation. As shown in Fig. 8a, pure FeWO₄ and ZnO could decompose 11% and 23% of RhB solution under irradiation for 150 min. As for ZnO, the degradation of RhB might be due to the dye-sensitized process.[34] While, in the case of ZnO modified FeWO₄ samples, the 1.5Zn–FWO₄ composite

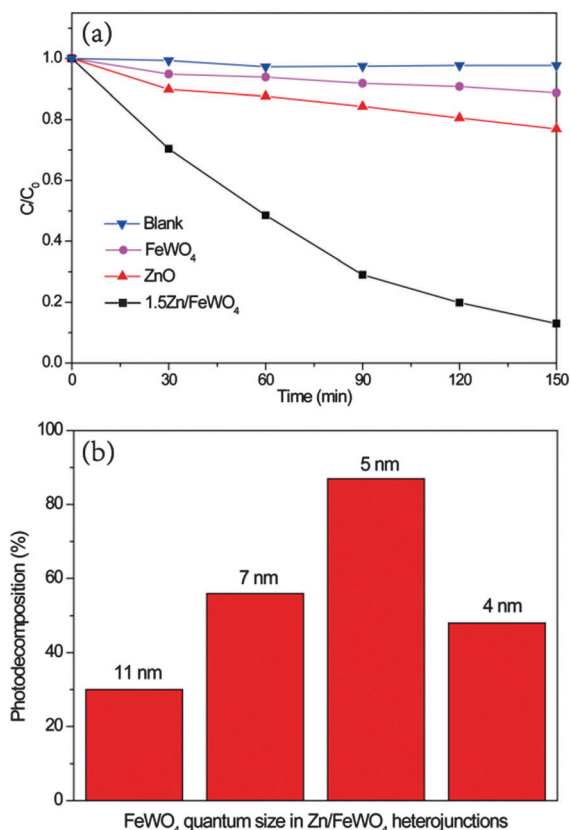Fig. 8 (a) Photocatalytic decomposition of RhB solution over different samples under visible light irradiation and (b) the effect of $FeWO_4$ size on the photocatalytic efficiencies of the ZnO modified $FeWO_4$ heterojunctions.

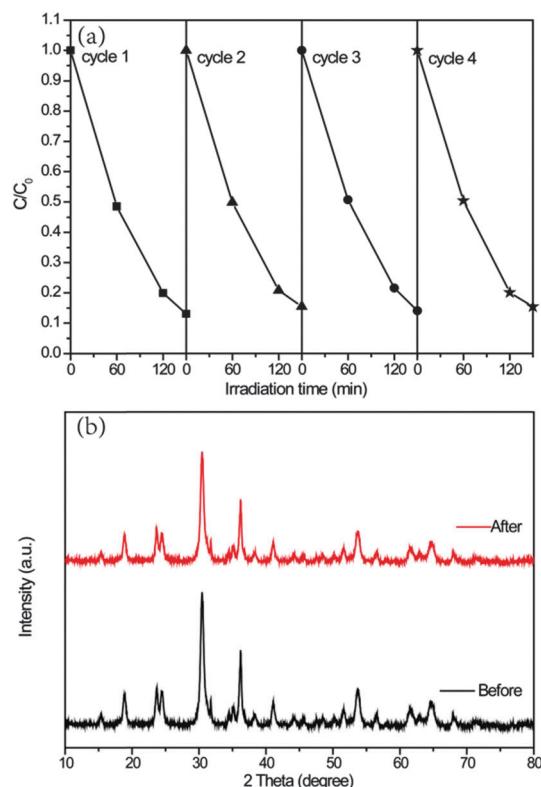Fig. 9 (a) Recycling tests of 1.5Zn–$FeWO_4$ under visible light irradiation and (b) XRD patterns of 1.5Zn–$FeWO_4$ before and after photocatalytic degradation of RhB solution with four cycles.

photocatalyst showed better activity than that of single $FeWO_4$ and ZnO. The absorption of RhB over 1.5Zn–FWO_4 significantly decreases with an increase of irradiation time (Fig. S6, ESI†). The intensity of the adsorption peak at 553 nm nearly disappears after 150 min. It also can be clearly seen that no corresponding increase in absorption is observed in the ultraviolet region, which indicates the complete destruction of most aromatic structures.[35] Besides, the correlation between the $FeWO_4$ quantum sizes and the photocatalytic performances of Zn–$FeWO_4$ is shown in Fig. 8b. It is found that Zn–$FeWO_4$ with 7 nm $FeWO_4$ nanoparticles exhibits the best photocatalytic performance. However, $FeWO_4$ nanoparticles with larger (7 nm) and smaller (4 nm) sizes make Zn–$FeWO_4$ with inferior photocatalytic performance.

The degradation kinetics of RhB under visible light irradiation over the as-obtained samples was investigated by the Langmuir–Hinshelwood model,[27] as shown in Fig. S7 (ESI†). The apparent rate constants for the prepared photocatalysts are summarized in Table S2 (ESI†). Especially, the decomposition of RhB over the 1.5Zn–FWO_4 heterojunction (0.0058 min^{-1}) is faster than that of $FeWO_4$ (0.0002 min^{-1}) and ZnO (0.0006 min^{-1}) by a factor of 29 and 9.7, respectively. To further confirm the heterojunction effect on the present system, the photocatalytic experiment of the M-1.5Zn–$FeWO_4$ sample is also investigated. The photocatalytic activity of the M-1.5Zn–$FeWO_4$ sample is much

lower than that of 1.5Zn–$FeWO_4$ (Fig. S8, ESI†). This result demonstrates that the 1.5Zn–$FeWO_4$ composite can form intimate interfaces in the heterojunction, rather than form loose interfaces in the mechanically mixed samples.[15,36]

In addition to photocatalytic efficiency, the stability of photocatalysts was another important factor for practical application.[37] The 1.5Zn–$FeWO_4$ heterojunction was recycled in four successive photocatalytic experiments. As shown in Fig. 9a, the photocatalytic activity of the 1.5Zn–$FeWO_4$ sample exhibits no significant loss after four recycles for the photodegradation of RhB solution. Fig. 9b presents the XRD patterns of 1.5Zn–$FeWO_4$ before and after four runs under visible light for the degradation of RhB solution. It can be clearly observed that the heterojunction is stable during the photocatalytic degradation process.

3.3. Photocatalytic mechanism

The activity of photocatalysts is mostly governed by the surface area, adsorption ability and separation efficiency of photogenerated carriers.[38] The comparison of the adsorption ability and reaction kinetics of photocatalytic degradation of the RhB dye in the presence of different products is shown in Fig. 10. Without visible irradiation, the adsorption ability of composite samples follows the trend: 1.5Zn–$FeWO_4$ > 0.5Zn–$FeWO_4$ > 2Zn–$FeWO_4$ > 1Zn–$FeWO_4$. However, the degradation rate does not follow the dye adsorption trend. The 1.5Zn–$FeWO_4$
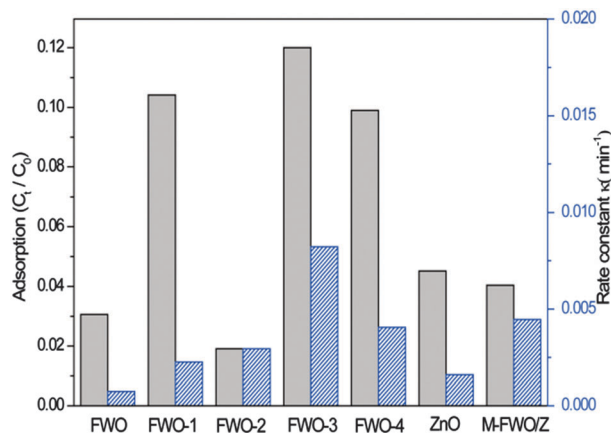
Fig. 10 Comparison of the reaction rate and adsorption ability of various photocatalysts: FeWO$_4$, 0.5Zn–FeWO$_4$, 1Zn–FeWO$_4$, 1.5Zn–FeWO$_4$, 2Zn–FeWO$_4$, ZnO and M-1.5Zn–FeWO$_4$.
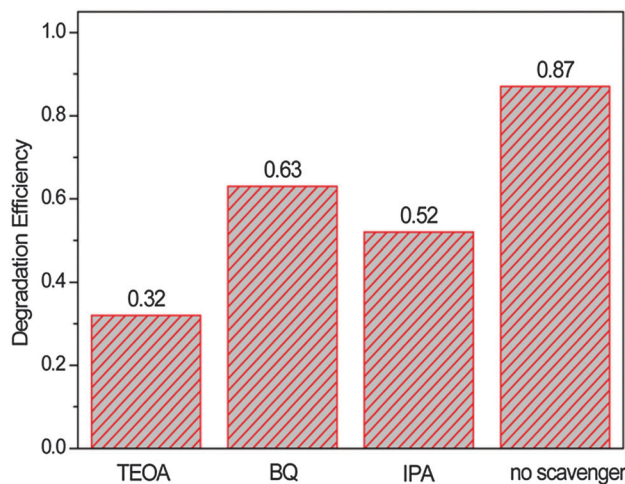

Fig. 11 Effects of different active scavengers on the degradation of RhB over the 1.5Zn–FeWO$_4$ composite.

heterojunction obviously showed higher photocatalytic activity under identical experimental conditions, followed by 2Zn–FeWO$_4$, and then 1Zn–FeWO$_4$ and 0.5Zn–FeWO$_4$. As a catalyst, the surface area is an important factor for its catalytic activity.[39,40] However, the N$_2$ adsorption–desorption measurements confirmed that the order of the photocatalytic performance of various photocatalysts is not consistent with the order of the surface area. That is to say, the enhanced photocatalytic activity is not due to the surface area but for other reasons. In this system, the enhancement of photocatalytic activity of the Zn–FeWO$_4$ heterojunction was mainly ascribed to efficient charge separation of photogenerated carriers.

The active species in the photocatalytic reactions of RhB were investigated by adding different scavengers, and the results are shown in Fig. 11. When triethanolamine (TEOA, a hole radical scavenger) is added into the reaction system, the degradation efficiency of RhB is obviously inhibited. When the benzoquinone (BQ) scavenger for superoxide radicals (O$_2^{\bullet-}$) is added into the reaction system, no obvious effect on the photocatalytic activity of 1.5Zn–FeWO$_4$ was observed. Moreover, once the isopropyl alcohol (IPA) scavenger for hydroxyl radicals is added to the reaction system, a slight inhibition phenomenon for photocatalytic reaction is observed. These results clearly suggest that the photocatalytic oxidation of RhB of the 1.5Zn–FeWO$_4$ heterojunction is mainly driven by photogenerated holes.[35] The O$_2^{\bullet-}$ plays a less important role than those of holes and hydroxyl radicals in photocatalytic oxidation of the RhB dye.

The energy band positions of FeWO$_4$ and ZnO were estimated according to the following empirical equations:[41]

$$E_{\mathrm{CB}} = X - E^{\mathrm{C}} - \tfrac{1}{2}E_g \qquad (2)$$

$$E_{\mathrm{VB}} = E_{\mathrm{CB}} + E_g \qquad (3)$$

where E_{VB} and E_{CB} are the valence band (VB) and conduction band (CB) edge potentials, respectively; X represents the absolute electronegativity of the semiconductor, which is defined as the geometric mean for absolute electronegativity of the constituent atoms. E^{C} is the energy of free electrons on the

hydrogen scale (about 4.5 eV), and E_g is the band gap energy of the semiconductor.[42] The energy band parameters of FeWO$_4$ and ZnO were calculated, and are listed in Table S3 (ESI†). Band position calculations suggest that ZnO and FeWO$_4$ have the staggered energy potentials that can reduce the combination of the photogenerated carriers between the two semiconductors.

Based on the above analysis results, we proposed the possible mechanism of enhanced photocatalytic activity of the Zn–FeWO$_4$ heterojunction. Schematic diagram of band energy positions and the charge transfer process of the Zn–FeWO$_4$ heterojunction under visible light irradiation are shown in Fig. 12. The positions of the CB bottom and the VB top of FeWO$_4$ (0.76 eV and 2.86 eV, respectively) are lower than those of ZnO (−0.40 eV and 2.80 eV, respectively). Besides, FeWO$_4$ could be simultaneously excited to form electron–hole pairs under visible light irradiation. Consequently, the photogenerated holes could easily transfer from the CB of FeWO$_4$ to that of ZnO, and further react with H$_2$O adsorbed on the surface of the heterojunction to produce $^\bullet$OH. Then the resulting $^\bullet$OH and a certain amount of h$^+$ could decompose the RhB dye to the final products. However, to continue the catalytic reaction, the electrons in the VB of FeWO$_4$ must be scavenged. Given the fact that the CB level of FeWO$_4$ (+0.76 eV vs. NHE) is more positive than $E_0(\mathrm{O}_2/\mathrm{O}_2^\bullet) = -0.046$ eV vs. NHE), adsorbed O$_2$ cannot be directly transferred to oxygen species by electrons in CB of FeWO$_4$. Hence, the electrons in the FeWO$_4$ CB are transported to the oxygen species through the multi-electron process.[43] Therefore, the electron–hole pairs were separated efficiently on the Zn–FeWO$_4$ heterojunction interface. On the other hand, as the sizes of FeWO$_4$ nanoparticles decrease, the band gaps of Zn–FeWO$_4$ become larger because of the quantum confinement of FeWO$_4$. However, the valence band of FeWO$_4$ shifts to more positive potentials resulting in the larger valence band energy difference between FeWO$_4$ and ZnO, which enhances the efficient transfer and the oxidation potential of holes.

Furthermore, in the process of RhB photosensitization, the electrons on the highest occupied molecular orbital (HOMO) of
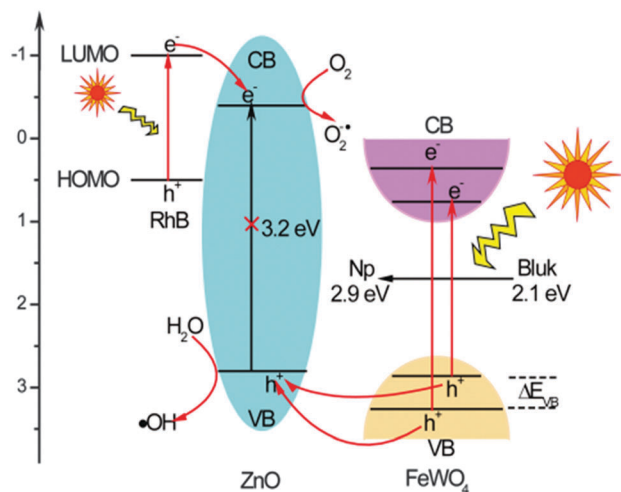
Fig. 12 Schematic diagram of band energy positions and the charge transfer process of the Zn–FeWO$_4$ heterojunction under visible light irradiation.

RhB molecules will be excited to the lowest unoccupied molecular orbital (LUMO) under visible light, and subsequently would be injected to the CB bottom of ZnO, further taking part in the degradation of RhB.

4. Conclusions

In summary, the mesoporous Zn–FeWO$_4$ heterojunctions with tunable band gaps have been successfully synthesized by a simple two-step method. ZnO nanoparticles were first prepared by calcination treatment of the precursors. And subsequently Zn–FeWO$_4$ heterojunctions were formed using a solvothermal process. SEM and TEM confirmed that the size of FeWO$_4$ was reduced by the modification of ZnO. Thus, the band gaps of FeWO$_4$ were significantly tuned, which can be demonstrated by the DRS analysis. The photocatalytic performance of Zn–FeWO$_4$ heterojunctions was better than that of pure FeWO$_4$ and ZnO. The optimal molar ratio of ZnO to FeWO$_4$ was 1.5 with the maximal photocatalytic degradation efficiency of 87% under the visible light irradiation for 3 h. The active species trapping experiments showed that the holes exhibited an obvious influence on the photocatalytic degradation process. Our preliminary experimental results showed that the remarkable enhancement of photocatalytic performance is mainly due to the efficient transfer and tunable band gaps. Moreover, this novel Zn–FeWO$_4$ heterojunction could be easily recycled several times, which is expected to show considerable potential application in wastewater treatment.

Acknowledgements

Notes and references

1 L. Zhang, S. Li, B. Liu, D. Wang and T. Xie, *ACS Catal.*, 2014, **4**, 12319.
2 H. Lin, L. Li, M. Zhao, X. Huang, X. Chen, G. Li and R. Yu, *J. Am. Chem. Soc.*, 2012, **134**, 8328.
3 P. Gao, A. Li, D. D. Sun and W. J. Ng, *J. Hazard. Mater.*, 2014, **279**, 96.
4 S. Li, J. Cai, X. Wu, F. Zheng, X. Lin, W. Liang, J. Chen, J. Zheng, Z. Lai, T. Chen and L. Zhu, *Appl. Catal., B*, 2014, **160–161**, 279.
5 Y. Wang, X. Guan, L. Li, H. Lin, X. Wang and G. Li, *New J. Chem.*, 2012, **36**, 1852.
6 Y. Chen, S. W. Park, B. K. Moon, B. C. Choi, J. H. Jeong and C. Guo, *CrystEngComm*, 2013, **15**, 8255.
7 J. Zhang, Y. Zhang, J.-Y. Yan, S.-K. Li, H.-S. Wang, F.-Z. Huang, Y.-H. Shen and A.-J. Xie, *J. Nanopart. Res.*, 2012, **14**, 1.
8 Y.-X. Zhou, Q. Zhang, J.-Y. Gong and S.-H. Yu, *J. Phys. Chem. C*, 2008, **112**, 13383.
9 J. Zhang, Y. Wang, S. Li, X. Wang, F. Huang, A. Xie and Y. Shen, *CrystEngComm*, 2011, **13**, 5744–5750.
10 F. Yu, L. Cao, J. Huang and J. Wu, *Ceram. Int.*, 2013, **39**, 4133.
11 Y.-X. Zhou, H.-B. Yao, Q. Zhang, J.-Y. Gong, S.-J. Liu and S.-H. Yu, *Inorg. Chem.*, 2009, **48**, 1082.
12 J. Guo, X. Zhou, Y. Lu, X. Zhang, S. Kuang and W. Hou, *J. Solid State Chem.*, 2012, **196**, 550.
13 S. Bera, S. B. Rawal, H. J. Kim and W. I. Lee, *ACS Appl. Mater. Interfaces*, 2014, **6**, 9654.
14 X. Cao, Y. Chen, S. Jiao, Z. Fang, M. Xu, X. Liu, L. Li, G. Pang and S. Feng, *Nanoscale*, 2014, **6**, 12366.
15 Y. Tian, B. Chang, J. Lu, J. Fu, F. Xi and X. Dong, *ACS Appl. Mater. Interfaces*, 2013, **5**, 7079.
16 A. Iwase, Y. H. Ng, Y. Ishiguro, A. Kudo and R. Amal, *J. Am. Chem. Soc.*, 2011, **133**, 11054.
17 Z. Wang, S.-W. Cao, S. C. J. Loo and C. Xue, *CrystEngComm*, 2013, **15**, 5688.
18 A. McLaren, T. Valdes-Solis, G. Li and S. C. Tsang, *J. Am. Chem. Soc.*, 2009, **131**, 12540.
19 Y. Wang, R. Shi, J. Lin and Y. Zhu, *Energy Environ. Sci.*, 2011, **4**, 2922.
20 S. Liu, M.-Q. Yang, Z.-R. Tang and Y.-J. Xu, *Nanoscale*, 2014, **6**, 7193.
21 X. Zou, H. Fan, Y. Tian and S. Yan, *CrystEngComm*, 2014, **16**, 1149.
22 L. Zheng, Y. Zheng, C. Chen, Y. Zhan, X. Lin, Q. Zheng, K. Wei and J. Zhu, *Inorg. Chem.*, 2009, **48**, 1819.
23 J. Jiang, X. Zhang, P. Sun and L. Zhang, *J. Phys. Chem. C*, 2011, **115**, 20555.
24 S. Balachandran, N. Prakash, K. Thirumalai, M. Muruganandham, M. Sillanpää and M. Swaminathan, *Ind. Eng. Chem. Res.*, 2014, **53**, 8346.
25 Y. Bai, P.-Q. Wang, J.-Y. Liu and X.-J. Liu, *RSC Adv.*, 2014, **4**, 19456.
26 S. Martha, K. H. Reddy and K. M. Parida, *J. Mater. Chem. A*, 2014, **2**, 3621.

27 K. H. Reddy, S. Martha and K. M. Parida, *Inorg. Chem.*, 2013, **52**, 6390.

28 W. Wang, L. Hu, J. Ge, Z. Hu, H. Sun, H. Sun, H. Zhang, H. Zhu and S. Jiao, *Chem. Mater.*, 2014, **26**, 3721.

29 J. Xu, M. Chen and Z. Wang, *Dalton Trans.*, 2014, **43**, 3537.

30 H. Cheng, B. Huang, X. Qin, X. Zhang and Y. Dai, *Chem. Commun.*, 2011, **48**, 97.

31 W. Zhao, Y. Wang, Y. Yang, J. Tang and Y. Yang, *Appl. Catal., B*, 2012, **115**, 90.

32 Z. Wu, L. Chen, C. Xing, D. Jiang, J. Xie and M. Chen, *Dalton Trans.*, 2013, **42**, 12980–12988.

33 F. Liu, Y. H. Leung, A. B. Djuriić, A. M. C. Ng and W. K. Chan, *J. Phys. Chem. C*, 2013, **117**, 12218.

34 J. Cao, B. Xu, H. Lin, B. Luo and S. Chen, *Dalton Trans.*, 2012, **41**, 11482.

35 H. Li, J. Liu, W. Hou, N. Du, R. Zhang and X. Tao, *Appl. Catal., B*, 2014, **160–161**, 89.

36 C. Chang, L. Zhu, S. Wang, X. Chu and L. Yue, *ACS Appl. Mater. Interfaces*, 2014, **6**, 5083.

37 Y. Yang, W. Guo, Y. Guo, Y. Zhao, X. Yuan and Y. Guo, *J. Hazard. Mater.*, 2014, **271**, 150.

38 L.-W. Zhang, H.-B. Fu and Y.-F. Zhu, *Adv. Funct. Mater.*, 2008, **18**, 2180.

39 F. Amano, K. Nogami, M. Tanaka and B. Ohtani, *Langmuir*, 2010, **26**, 7174.

40 N. M. Flores, U. Pal, R. Galeazzi and A. Sandoval, *RSC Adv.*, 2014, **4**, 41099.

41 H.-q. Jiang, H. Endo, H. Natori, M. Nagai and K. Kobayashi, *Mater. Res. Bull.*, 2009, **44**, 700.

42 D.-K. Ma, M.-L. Guan, S.-S. Liu, Y.-Q. Zhang, C.-W. Zhang, Y.-X. He and S.-M. Huang, *Dalton Trans.*, 2012, **41**, 5581.

43 L. Ye, J. Liu, Z. Jiang, T. Peng and L. Zan, *Appl. Catal., B*, 2013, **142–143**, 1.